Nanoscale

PAPER

View Article Online
View Journal | View Issue

Cite this: *Nanoscale*, 2025, **17**, 10743

Superior photoconversion efficiency of nanocrystal sensitized solar cells based on all-inorganic $CsPbX_3$ (X = Br, I) perovskites†

Baidyanath Roy,[a] Tamal Dey, ‡[a] Shaona Bose,[b] Somnath Mahato, [c] Narayan Chandra Das[d] and Samit K. Ray *[b]

Nanocrystal-sensitized solar cells have emerged as potential alternatives to traditional photovoltaic technology due to their unique light absorption and emission characteristics and size-dependent bandgap. In this work, we report the successful synthesis of cubic-phase $CsPbI_3$ and $CsPbBr_3$ nanocrystals for their use as photosensitizers in solar cells, referred to as perovskite nanocrystal-sensitized solar cells (PNCSSCs). Among the two systems, $CsPbI_3$ is found to be superior for PNCSSCs because of its high absorption efficiency, lower bandgap, and higher photoluminescence yield, as compared to $CsPbBr_3$. Our study examines the structural, compositional, optical, and electrical properties of these perovskite nanocrystals, focusing on their contributions to photoconversion efficiency. $CsPbBr_3$ nanocrystals exhibit a band gap of ~2.4 eV along with defect states-induced short carrier lifetime of around 18 ns. In contrast, $CsPbI_3$ demonstrates a band gap of ~1.8 eV closer to the peak of the solar spectrum with a much longer carrier lifetime of ~130 ns, which facilitates better separation and collection of photogenerated charge carriers. Consequently, $CsPbI_3$ nanocrystal-sensitized solar cells fabricated with mesoporous TiO_2 reveal a photoconversion efficiency of ~12.5%, as compared to 3.8% for $CsPbBr_3$ nanocrystal solar cells. To the best of our knowledge, this is the highest reported photoconversion efficiency in solution-processed perovskite nanocrystal-sensitized solar cells.

Received 12th November 2024,
Accepted 26th March 2025

DOI: 10.1039/d4nr04752d

rsc.li/nanoscale

Introduction

The pursuit of sustainable energy solutions is of paramount focus in scientific research, with particular emphasis on solar energy due to its abundance and renewability. In the array of photovoltaic technologies, dye-sensitized solar cells (DSSCs) have emerged as a promising option, largely due to their relatively simple fabrication process, lower costs, and flexibility in design compared to traditional silicon-based solar cells.[1–4] DSSCs are primarily based on a photo-sensitization process, where a photosensitive dye absorbs photons to initiate electron transfer, converting solar energy into electrical energy. Although DSSCs have achieved significant progress in power conversion efficiencies (PCE), limitations in light absorption range, availability of environment-friendly dyes, and stability continue to restrain their progress. This has driven the exploration of alternative materials as photo-sensitizers, with semiconducting nanocrystals (NCs) as the focus due to their unique electronic and optical properties.[5–7] NCs offer distinct advantages over traditional organic dyes used in DSSCs. The quantum confinement effects, arising from nanoscale dimensions, allow tunability of the band gap by adjusting the size of the particles, enabling a much broader absorption across the solar spectrum and thereby enhancing light-harvesting capabilities.[8] The inherent operational stability of NCs also addresses one of the significant challenges faced by organic dyes, which often suffer from photodegradation, limiting the operational lifetime of DSSCs.[8,9] These unique attributes in the solution-processed nanocrystal-sensitized solar cells (NCSSCs) have the potential to surpass the limitations of conventional DSSCs and offer new pathways to efficient, stable, and cost-effective photovoltaic devices.

Among the various semiconductor NCs under investigation, all-inorganic lead halide perovskites, specifically cesium lead

[a]*School of Nano Science and Technology, Indian Institute of Technology, Kharagpur, West Bengal 721302, India*
[b]*Department of Physics, Indian Institute of Technology, Kharagpur, West Bengal 721302, India. E-mail: physkr@phy.iitkgp.ac.in*
[c]*Łukasiewicz Research Network-PORT Polish Centre for Technology Development, Stabłowicka 147, 54-066 Wrocław, Poland*
[d]*Rubber Technology Centre, Indian Institute of Technology, Kharagpur, West Bengal 721302, India*

†Electronic supplementary information (ESI) available. See DOI: https://doi.org/10.1039/d4nr04752d

‡Currently at the Department of Electrical & Computer Engineering, Rutgers, The State University of New Jersey, Piscataway, New Jersey 08854, United States.

bromide ($CsPbBr_3$) and cesium lead iodide ($CsPbI_3$), have attracted considerable attention as potential candidates for photosensitizers in DSSCs.[10–12] These materials exhibit remarkable optoelectronic properties such as high photoluminescence quantum yields, tunable band gaps, and superior charge carrier mobility.[13,14] $CsPbBr_3$, with a large band gap of ~2.4 eV, is highly suited for use in tandem cells and high-power device applications, while $CsPbI_3$, with a narrower band gap of ~1.8 eV, exhibits an absorption profile better matched to the solar spectrum peak, making it ideal for applications requiring efficient light absorption and conversion.[15–18] Their tunable electronic structures and efficient charge transport properties are conducive to enhanced photogenerated charge separation and reduced recombination, which are critical for achieving high photoconversion efficiency (PCE) in solar cells. Moreover, the synthesis of $CsPbBr_3$ and $CsPbI_3$ NCs can be precisely controlled to produce nanoparticles with well-defined size and morphology, enabling optimization of their performance in solar cell applications. The inorganic nature of these NCs also offers improved thermal and environmental stability over their hybrid perovskite counterpart, a crucial factor for the longevity of solar cells operating in diverse climate conditions.[19,20]

This investigation provides a comprehensive analysis of the role of $CsPbBr_3$ and $CsPbI_3$ NCs as sensitizers in solar cells, also referred to as perovskite nanocrystal-sensitized solar cells (PNCSSCs), focusing on their synthesis, structural characterization, optoelectronic and charge transfer properties, and device performance. We explore how these materials have the potential to elevate the efficiency and stability of NCSSCs, bridging the gap between laboratory research and commercial application. This study also takes into account the challenges associated with their commercialization, owing to issues of toxicity, scalability, and stability, and discusses recent advancements aimed at addressing these obstacles. Through this investigation, we seek to illustrate how $CsPbBr_3$ and $CsPbI_3$ NCs contribute to the ongoing evolution of solar cell technologies and their implications on the future of renewable energy solutions.

Experimental section

Synthesis of $CsPbI_3$ and $CsPbBr_3$ nanocrystals

$CsPbI_3$ and $CsPbBr_3$ nanocrystals (NCs) were synthesized using the hot injection method.[13,21] Lead bromide ($PbBr_2$) and lead iodide (PbI_2) were each prepared in a concentration of 0.005 M in a two-neck round-bottom flask with octadecene as the solvent. The flask was heated at 150 °C for one hour to remove dissolved oxygen and moisture under vacuum. Then nitrogen gas (N_2) was introduced to maintain an inert environment while allowing complete dissolution of the lead halides. Once dissolved, 1 ml of oleic acid (OA) and 1 ml of oleylamine (OLAm) were added. OA converts the lead precursor to lead oleate, while OLAm further solubilizes the complex by forming an OLAm-X adduct, acting as both a halogen source and a stabilizing ligand for the NCs. Next, a pre-heated solution of cesium oleate (Cs-OA) was injected into the reaction mixture. This solution was previously prepared by dissolving a 0.0005 M concentration of cesium carbonate (Cs_2CO_3) in 40 ml of octadecene and 4 ml OA and heating them at 150 °C for 1 hour in an inert atmosphere. After injection of 4 ml Cs-OA, the reaction mixture was quickly quenched in an ice bath to freeze further nucleation of NCs. The resulting solution was centrifuged and refrigerated for further characterization and device fabrication.

Materials characterisation

The crystallographic structure of the perovskites was investigated by using the BRUKER D8 – FOCUS X-Ray diffractometer with incident Cu-K_α radiation (k = 1.5406 Å). The transmission electron microscope (TEM) images were taken using the FEI Tecnai G2 20 TWIN is a 200 kV TEM. The electronic states of the perovskites were analyzed by XPS in a PHI 5000 Versa Probe-II (ULVAC, PHI, Inc.) spectrometer equipped with a monochromatic Al-K_α X-ray source having an energy of 1486.6 eV and base pressure ~2.6×10^{-6} Pascal. Absorption spectra of the films spin-coated on cleaned glass substrates were measured using UV–A visible light range absorption spectrophotometer (U-2910 Spectrophotometer, HITACHI). Photoluminescence spectra were recorded using a Triax-320 monochromator equipped with a photomultiplier tube (Hamamatsu R928) and 325 nm laser excitation.

Device fabrication and testing

To fabricate the PNCSSCs, pre-cleaned fluorine-doped tin oxide (FTO) coated glass substrates were used as transparent electrodes. A uniform layer of commercially sourced TiO_2 paste from Sigma-Aldrich was applied on the FTO substrates using the doctor-blade technique, ensuring uniform coverage. The TiO_2-coated substrates were then subjected to a gradual ramp heating process till 450 °C to transform the TiO_2 film into a mesoporous structure. This mesoporous texture enhances the surface area available for the adsorption of perovskite NCs, facilitating better contact between the NCs and the TiO_2 layer. After preparing the mesoporous TiO_2 layer, the FTO substrates were immersed in the as-synthesized $CsPbBr_3$ and $CsPbI_3$ solutions for 24 hours, allowing the perovskite NCs to adsorb onto the TiO_2 surface. Next, the substrates were gently rinsed with ethanol to remove any unbound NCs and then dried in ambient conditions to prepare them for subsequent assembly steps. Separately, a solution of H_2PtCl_6 (2 wt%) was spin-coated onto another clean FTO-coated glass substrate and subsequently dried at 90 °C for two hours. This step was followed by annealing the substrate at 450 °C, which promoted the formation of platinum nanoparticles on the FTO surface. In this nanoparticulate form, platinum acts as an effective catalyst for regenerating the electrolyte redox couple, with enhanced catalytic activity due to its increased surface area. For the electrolyte preparation, a redox couple was formed by dissolving 0.1 M lithium iodide (LiI), 0.05 M iodine (I_2), 0.5 M *t*-butyl pyridine, and 0.6 M DMP-II (1,2-dimethyl-3-propylimidazolium

iodide) in 10 ml of acetonitrile. This mixture was stirred under dark conditions at room temperature for approximately 5–6 hours to ensure the formation of an I_3^-/I^- redox couple, a crucial component for efficient device operation. To assemble the device, the TiO_2-coated FTO glass substrates, and the Pt-nanoparticle-coated counter electrodes were aligned and held together like a sandwich with paper clips. A pipette was used to introduce the prepared electrolyte solution along the junction between the electrodes. Finally, the entire device structure was sealed along its edges to enhance stability and prevent the evaporation of the electrolyte, preparing the device for electrical measurements and further testing. The assembled perovskite QD-sensitized solar cells were tested under a solar simulator. Electrical characterization was performed with a Keithley semiconductor parameter analyzer (4200A-SCS). Impedance spectroscopy was carried out with Gamry Instruments in a two-electrode measurement configuration.

Results and discussion

The formation of crystalline phases and particle sizes of $CsPbBr_3$ and $CsPbI_3$ nanocrystals (NCs) have been analyzed using X-ray diffraction (XRD). Characteristic diffraction peaks are observed at 14.2°, 20.5°, and 28.4° in $CsPbI_3$, corresponding to the (100), (110), and (200) planes, respectively, confirming the formation of cubic phase perovskite in the form of a superlattice structure,[22] as shown in Fig. 1(a). A transmission electron microscopy (TEM) image of a $CsPbI_3$ QD is shown in Fig. 1(b) with dimensions ~17 nm, showing cubic shape of NCs. Since the reported average sizes of $CsPbI_3$ and $CsPbBr_3$ (~17 nm and ~13 nm) are larger than the excitonic Bohr radius (7 nm and 12 nm for $CsPbBr_3$ and $CsPbI_3$, respectively[23]), they may not exhibit strong quantum confinement effects. However, they could still experience some degree of confinement compared to their bulk counterparts. Quantum confinement in $CsPbBr_3$ and $CsPbI_3$ perovskite nanocrystals significantly influences their morphology, stability, bandgap, and optical properties. In the case of quantum confinement, as the nanocrystal size decreases, the bandgap widens, leading to a blue shift in photoluminescence and enhanced quantum yield. From TEM images in Fig. 1, the sizes of our NCs are larger than the Bohr excitonic radius of $CsPbX_3$ (X = Br and I), so they may not exhibit strong quantum confinement effect.[24,25] However, weak confinement with uniform nanocrystal size distribution results in very high photoluminescence intensity[26] with a slight blue shift in peak position, as we present later in Fig. 2(b) and (e). High-resolution TEM (HRTEM) image shown in Fig. 1(c) of the $CsPbI_3$ QD depicts an interplanar spacing of ~0.65 nm. In comparison, XRD

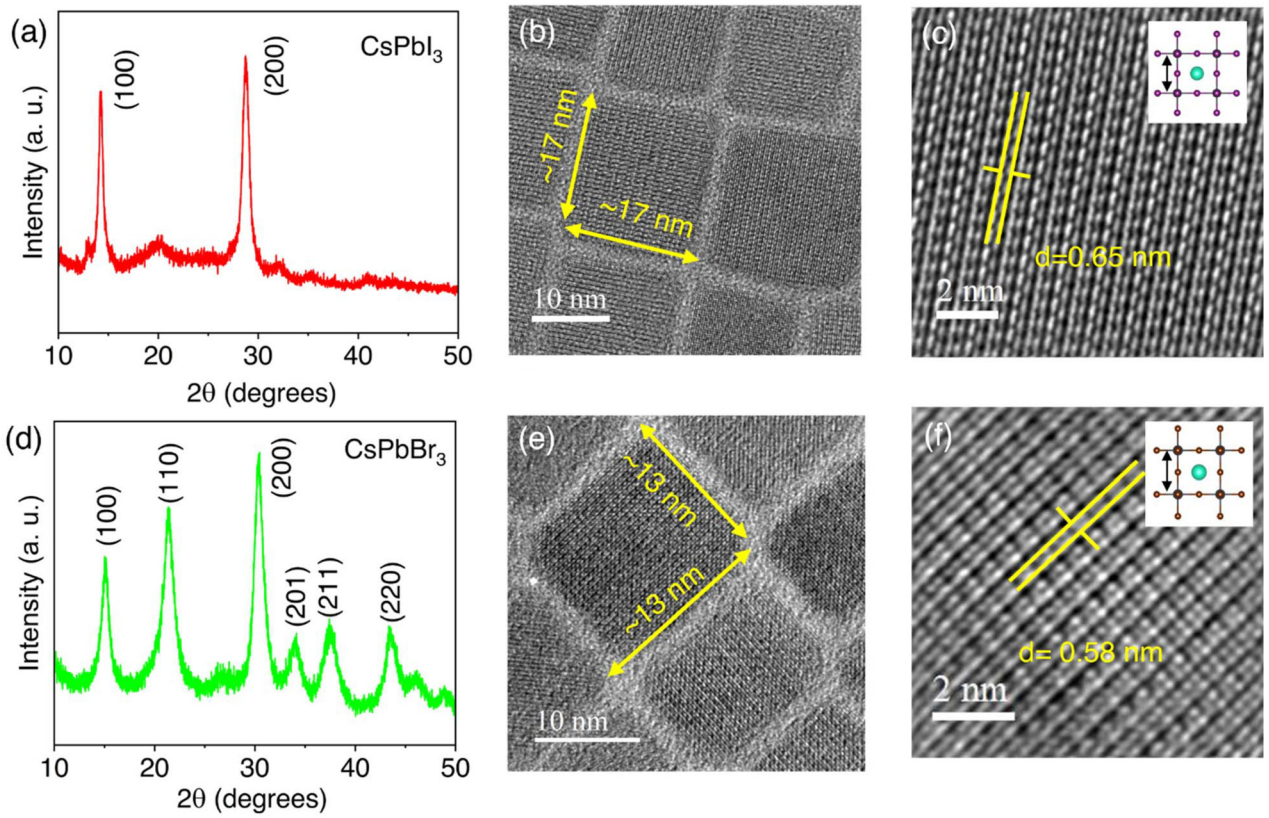

Fig. 1 (a) X-ray diffraction pattern, (b) TEM image, and (c) HRTEM image of as-synthesized $CsPbI_3$ nanocrystals (NCs). (d) X-ray diffraction pattern, (e) TEM image, and (f) HRTEM image of as-synthesized $CsPbBr_3$ NCs.

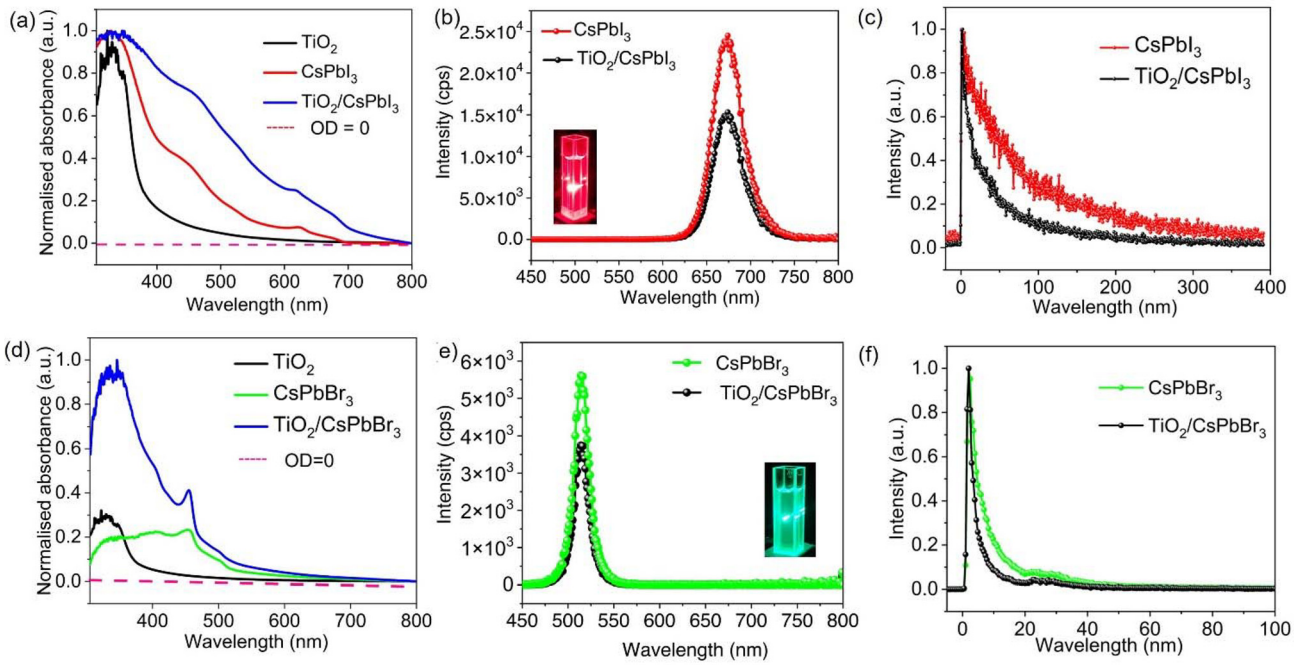

Fig. 2 (a) Absorption spectra of TiO_2, $CsPbI_3$ and $CsPbI_3$ coated mesoporous TiO_2. (b) PL spectra of $CsPbI_3$ and $TiO_2/CsPbI_3$ showing PL quenching effect and (c) PL decay curves of $CsPbI_3$ and $TiO_2/CsPbI_3$ NCs. (d) Absorption spectra of TiO_2, $CsPbBr_3$ and $CsPbr_3$ coated mesoporous TiO_2. (e) PL spectra showing PL quenching effect and (f) PL decay curves of $CsPbBr_3$ and $TiO_2/CsPbBr_3$ NCs.

peaks observed at 15.1°, 21.3°, and 30.2° corresponding to the (100), (110), and (200) planes of $CsPbBr_3$, shown in Fig. 1(d), are at slightly higher diffraction angles than those of $CsPbI_3$. As Br is a smaller-sized atom than I, the interplanar spacing is decreased in $CsPbBr_3$ and thus appears at higher values of 2θ. A TEM image of the $CsPbBr_3$ NCs with dimensions ~13 nm is shown in Fig. 1(e) with corresponding interplanar spacing of 0.58 nm in Fig. 1(f).

UV-Vis absorption spectra in Fig. 2(a) and (d) show peaks around 700 nm and 510 nm for $CsPbI_3$ and $CsPbBr_3$, respectively. Tauc plots, given in Fig. S1,† indicate bandgaps of 1.8 eV and 2.4 eV for $CsPbI_3$ and $CsPbBr_3$, respectively, suggesting that $CsPbI_3$ has superior visible-light absorption capability. Photoluminescence (PL) measurements reveal emission peaks at 675 nm for $CsPbI_3$ (red) and 510 nm for $CsPbBr_3$ (green) in Fig. 2(b) and (e), indicating potential applications for $CsPbI_3$ in solar cells due to its broader absorption range, closer to the peak of the solar spectrum. When these NCs are adsorbed on mesoporous TiO_2, their PL intensity is strongly quenched, as depicted in the respective figures. This suggests charge transfer from perovskite NCs to TiO_2. PL decay studies shown in Fig. 2(c) and (f) demonstrate a bi-exponential decay (solid line representing the fitted experimental data points as depicted in Fig. S2 and S3†) of photogenerated carriers, where the longer carrier lifetime (τ) represents radiative decay, and the shorter lifetime indicates nonradiative decay. The radiative carrier lifetimes are extracted to be approximately 130 ns for $CsPbI_3$ and 18 ns for $CsPbBr_3$. When $CsPbI_3$ is interfaced with TiO_2, the lifetime reduces to 59 ns, whereas that in $CsPbBr_3/TiO_2$ reduces to 9 ns. This reveals more efficient charge transfer in $CsPbI_3/TiO_2$ than in $CsPbBr_3/TiO_2$, demonstrating more efficient charge extraction for $CsPbI_3$-based PNCSSCs. It is also to be noted that the observed bumps in Fig. 2(f) are due to the defects or trap states in the $CsPbBr_3$ nanocrystals[27] that can capture charge carriers. The subsequent release of these carriers may lead to delayed photoluminescence, appearing as bumps in the decay profile.[28]

Typical high-resolution X-ray photoelectron spectroscopy (XPS) spectra of Cs_{3d}, Pb_{4f}, I_{3d}, and Br_{3d} electrons in Fig. 3 depict the nature of local chemical bonding of synthesized perovskite NCs. The binding energies (BE) of Cs $3d_{5/2}$ and $3d_{3/2}$ core electrons in $CsPbI_3$ are found to be at 722.8 eV and 736.8 eV respectively. These values are found to be increased to 723.5 and 737.6 eV, respectively, in $CsPbBr_3$, owing to the smaller size of Br atoms. The BE values of Pb $4f_{7/2}$ and $4f_{5/2}$ electrons in $CsPbI_3$ are 136.7 and 141.5 eV, respectively, whereas those in $CsPbBr_3$ are 137.6 and 142.6 eV respectively, as depicted in Fig. 3(b). Fig. 3(c) shows I $3d_{5/2}$ and $3d_{3/2}$ peaks of $CsPbI_3$ at 618.2 eV and 629.7 eV, respectively. On the other hand, Br 3d XPS peak in as-synthesized $CsPbBr_3$ has been deconvoluted to extract the BE of Br $3d_{5/2}$ and $3d_{3/2}$ electrons and are found to be 67.6 and 68.5 eV, respectively. These BE values are in close agreement with the reported data,[29,30] indicating phase purity of synthesized $CsPbBr_3$ and $CsPbI_3$ nanocrystals.

The as-synthesized $CsPbBr_3$ and $CsPbI_3$ NCs have been incorporated as photosensitizer materials as an alternative to traditional dyes used in dye-sensitized solar cells. A schematic

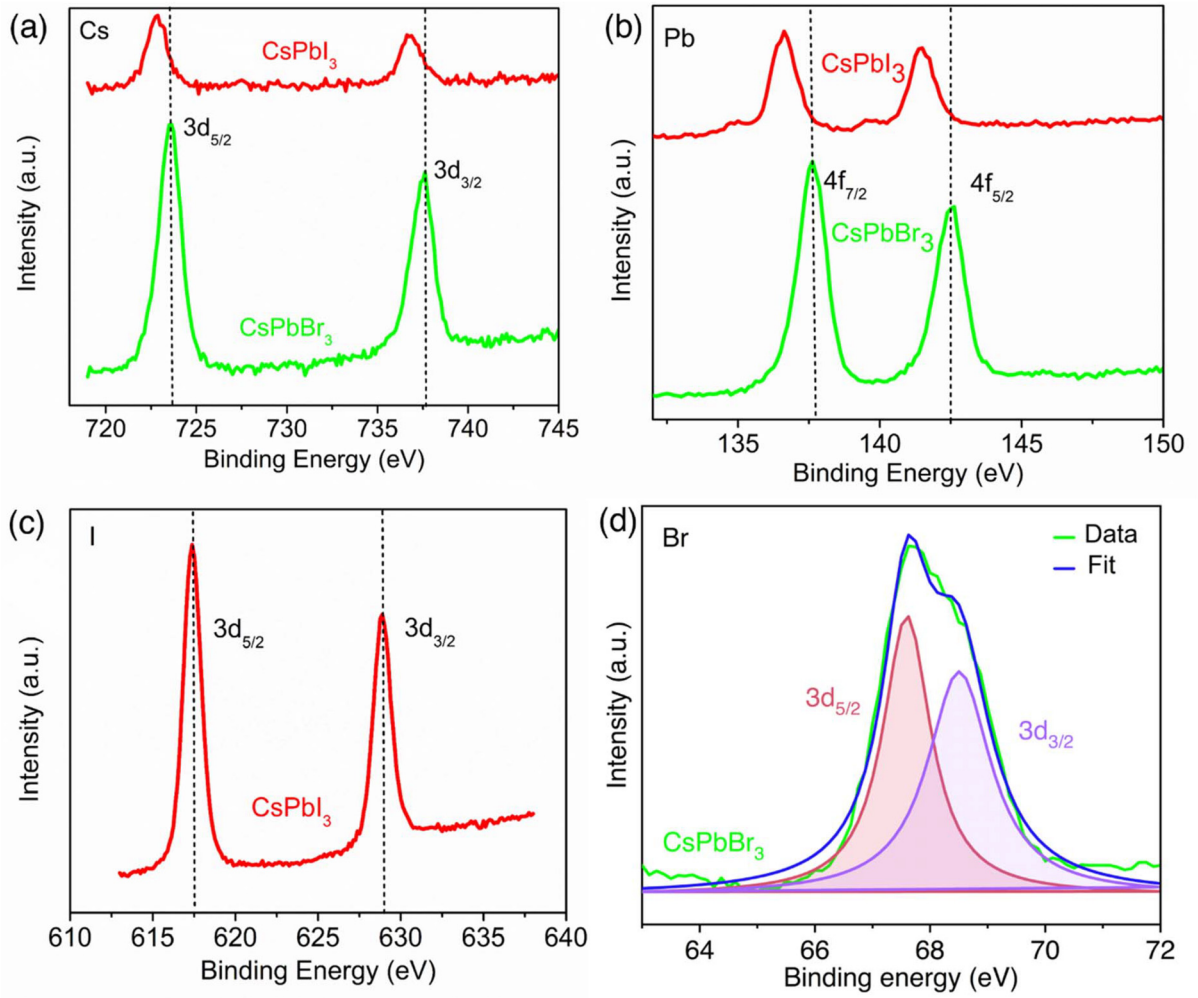

Fig. 3 High-resolution XPS spectra of (a) Cs, (b) Pb, (c) I, and (d) Br core electrons of as-synthesized $CsPbI_3$ and $CsPbBr_3$ NCs.

of the fabricated perovskite nanocrystal-sensitized solar cells (PNCSSCs) is shown in Fig. 4(a). In this study, fluorine-doped tin oxide (FTO) has been chosen as the transparent conducting electrode due to its lower sheet resistance and greater thermal stability compared to indium-doped tin oxide (ITO).[31] These properties make FTO a reliable choice for high-performance solar cell applications that require stable conductivity under elevated temperatures.[31,32] A mesoporous layer of TiO_2, the morphology of which is shown in Fig. S4(a),† has been deposited onto the FTO substrate to serve as a sensitizing medium, leveraging its high surface area and excellent electron transfer capabilities, which facilitate efficient electron transport from the sensitizer to the conductive substrate. The design of the PNCSSC incorporates a redox electrolyte based on the I_3^-/I^- redox couple, $CsPbBr_3$ and $CsPbI_3$ NCs as sensitizing agents, and platinum (Pt) as the counter electrode. The resulting configuration of the device shown in Fig. 4(a) is a multilayered structure represented as FTO/m-TiO_2/perovskite NCs/Pt/FTO. The NCs are adsorbed onto the surface of the mesoporous TiO_2 layer (Fig. S2(b)†), where they play a central role in capturing incident sunlight to generate photo-excited electrons, which are then injected into the conduction band of TiO_2, a process that enables solar energy conversion. The efficiency of the photoconversion process in these solar cells is influenced by several critical parameters, including the energy levels of the excited states (LUMO) and ground state (HOMO) of the NCs, the Fermi level of the Pt anode, and the redox potential of the I_3^-/I^- electrolyte. Together, these factors govern the energetics of electron transfer and the overall efficiency of the device's electrochemical reactions. The photoconversion mechanisms in I-based perovskite are given below.[33]

$$NCs + h\upsilon = NCs^* \ldots \quad (1)$$

$$NCs^* + Pt\ (CE) = NCs^+ + e^-{}_{CB}\ (Pt) \ldots \quad (2)$$

$$NCs^+ + 3I^-(electrolyte) = NCs + I^{3-} \ldots \quad (3)$$

$$I^{3-} + 2e^-(catalysts) = 3I^-(electrolyte\ regeneration) \ldots \quad (4)$$

Fig. 4(b) illustrates the energy band alignment for $CsPbBr_3$ and $CsPbI_3$ PNCSSCs, revealing critical differences in electron migration behavior between the two sensitizer materials.

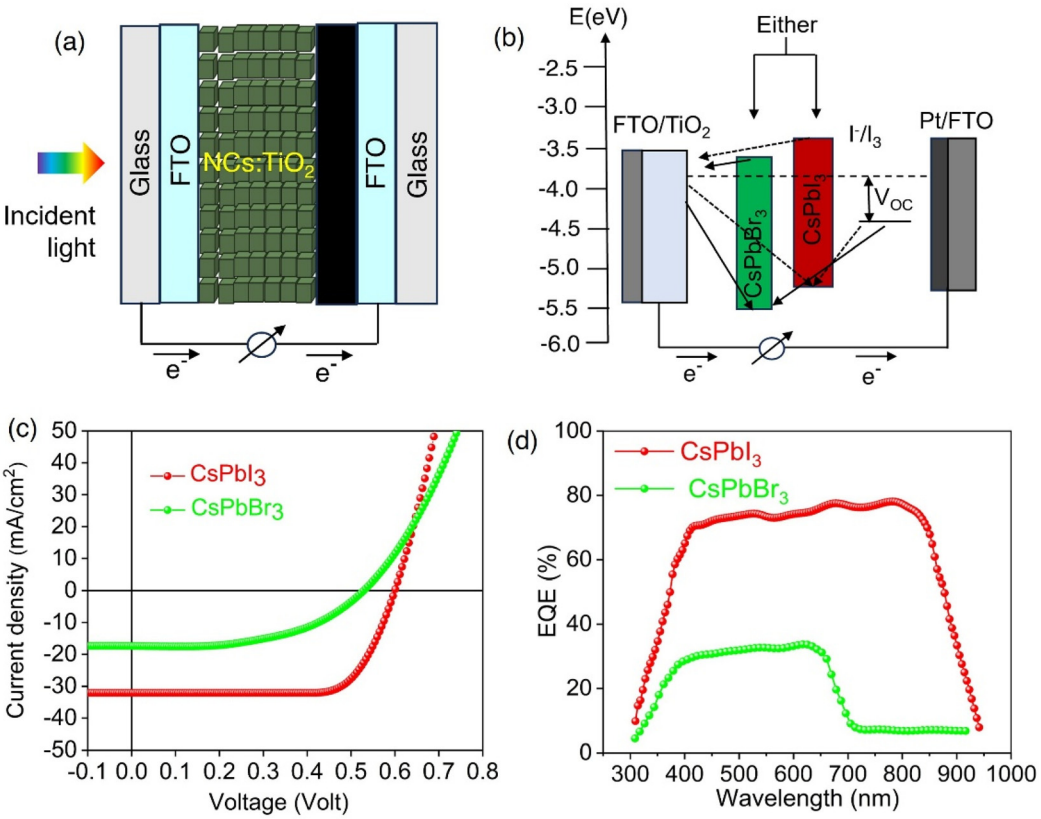

Fig. 4 (a) Schematic diagram of nanocrystal sensitized solar cell based on $CsPbI_3$ and $CsPbBr_3$, (b) corresponding energy band diagram of the solar cell using $CsPbI_3$ and $CsPbBr_3$ nanocrystals adsorbed on mesoporous TiO_2. (c) Photovoltaic characteristic of the devices representing the short circuit current density and open circuit voltage of $CsPbI_3$ and $CsPbBr_3$ nanocrystals sensitized devices and (d) external quantum efficiency (EQE) of fabricated perovskite nanocrystals sensitized solar cells.

Devices with both materials are shown in the same schematic for comparison. The $CsPbBr_3$ layer is shown in green, and the $CsPbI_3$ layer is shown in red. Fig. 4(c) shows the current density–voltage (J–V) characteristics of the devices. $CsPbI_3$-based solar cells exhibit a higher short circuit current density (J_{sc}), higher open circuit voltage (V_{oc}), and greater fill factor (FF). These lead to a significantly higher photoconversion efficiency (PCE) for $CsPbI_3$ NCs sensitized solar cells. It is evident from the band alignment in Fig. 4(b) that electron transfer from $CsPbI_3$ to TiO_2 is energetically more favorable compared to that of $CsPbBr_3$. This favorable transport pathway facilitates efficient electron injection into the TiO_2 conduction band, which is essential for enhancing the overall charge carrier dynamics within the cell. Additionally, $CsPbI_3$ demonstrates superior photon absorption capability in the solar spectrum relative to $CsPbBr_3$, which leads to a higher generation rate of photo-induced charge carriers. The increased absorption efficiency enables enhanced harvesting of incident light, thus producing a higher density of charge carriers available for transfer. A combination of these factors, *i.e.*, favorable band alignment for electron transport and the increased photo-absorbed charge carrier density in $CsPbI_3$, may result in an enhanced charge collection at the electrodes, directly impacting the photoconversion efficiency.

A Newport solar simulator working at Solar Air Mass (AM) 1.5 G conditions, equivalent to 100 mW cm^{-2} of irradiance, has been used for photovoltaic measurements. When exposed to illumination, the $CsPbI_3$ sensitized champion solar cell demonstrates an open-circuit voltage (V_{oc}) of approximately 0.60 V, in contrast to the $CsPbBr_3$ sensitized cell, which shows a V_{oc} of ~0.53 V. There is also a notable increase of approximately 70% in the short-circuit current density (J_{sc}) for the $CsPbI_3$ device, reaching 31.9 mA cm^{-2} compared to 17.3 mA cm^{-2} for the $CsPbBr_3$ based cell. This substantial improvement in both J_{sc} and V_{oc} values for $CsPbI_3$ is attributed to the enhanced generation of photogenerated charge carriers, longer carrier lifetimes, and greater conductivity due to favorable band alignment in the $CsPbI_3$ device. Furthermore, the fill factor (FF) for the $CsPbI_3$-based solar cell is calculated to be ~65%, significantly higher than the 41% observed for the $CsPbBr_3$ cell, which reflects a greater maximum power output potential. We obtained a PCE of 3.7% and 12.5% in the $CsPbBr_3$ and $CsPbI_3$-based PNCSSCs, respectively. The calculated photovoltaic device parameters are presented in Table 1. Fig. S5(a and b)† shows the repeatability of ten numbers of $CsPbBr_3$ and $CsPbI_3$ sensitized solar cells. In Fig. S6,† a detailed statistical analysis of PCE from ten devices is given as a table, as well as charts with error bars.

Table 1 Comparison of perovskite nanocrystals sensitized solar cell device parameters

Active materials	J_{sc} (mA cm^{-2})	V_{oc} (volt)	FF (%)	PCE (%)
$CsPbBr_3$	17.3	0.53	41	**3.7%**
$CsPbI_3$	31.9	0.60	65	**12.5%**

The external quantum efficiency (EQE) spectra for both $CsPbI_3$ and $CsPbBr_3$ sensitized solar cells are illustrated in Fig. 4(d). As anticipated, the EQE of the $CsPbI_3$ device is notably higher, which is due to its superior optical absorption coefficient and efficient separation and collection of photogenerated carriers in comparison to the $CsPbBr_3$ cell.

To explain the improved fill factor of $CsPbI_3$ sensitized solar cells, electrochemical impedance spectroscopy (EIS)[34] of the devices have been performed. EIS plays a crucial role in explaining the fill factor (FF) in sensitized solar cells, as it provides insights into the internal resistance mechanisms and charge transport dynamics within the cell. The FF is a key performance metric of a solar cell that represents the ratio of the maximum power output to the theoretical power from the product of open-circuit voltage and short-circuit current density. Analyzing EIS data allows us to dissect and quantify the resistive and capacitive elements within the device, which ultimately impact the FF. In sensitized solar cells, such as dye-sensitized or perovskite-sensitized ones, multiple interfaces exist where charge transfer occurs, including interfaces between the sensitizer and the semiconductor (*e.g.*, dye or perovskite/TiO_2), the interface between the sensitizer and the electrolyte or hole transport layer (HTL) electrode where electrons and holes are extracted. By applying EIS, we can evaluate the impedance spectrum over a range of frequencies. The results help in isolating the charge transfer resistance (R_{ct}) at these interfaces. Lower R_{ct} typically indicates more efficient charge injection from the sensitizer to the semiconductor and then from the semiconductor to the electrodes, thereby minimizing energy losses. As the FF is sensitive to losses within the cell, a lower R_{ct} is beneficial for achieving a higher FF.[35] In addition to the charge transfer resistance, EIS provides information on series resistance (R_s), which arises from the conductive elements within the solar cell, such as the transparent conductive oxide (TCO) layer, the semiconductor layer, and the metal contacts. High series resistance can impede the flow of photogenerated charges, resulting in voltage drops and lowering the maximum power output of the solar cell.[36] The fill factor is particularly sensitive to R_s because higher series resistance reduces the curvature of the current–voltage (I–V) characteristics, thereby reducing the achievable maximum power point. Through EIS, the R_s can be accurately quantified, enabling the identification of sources contributing to this resistance. Lowering R_s through improved material quality, better conductivity in the contacts, or optimized layer thickness can directly lead to higher FF. Therefore, understanding R_s through EIS helps engineers design cells with minimal resistive losses, enhancing the FF. EIS data and their analysis for PNCSSCs are presented in Fig. 5. Fig. 5(a) shows the typical model used to

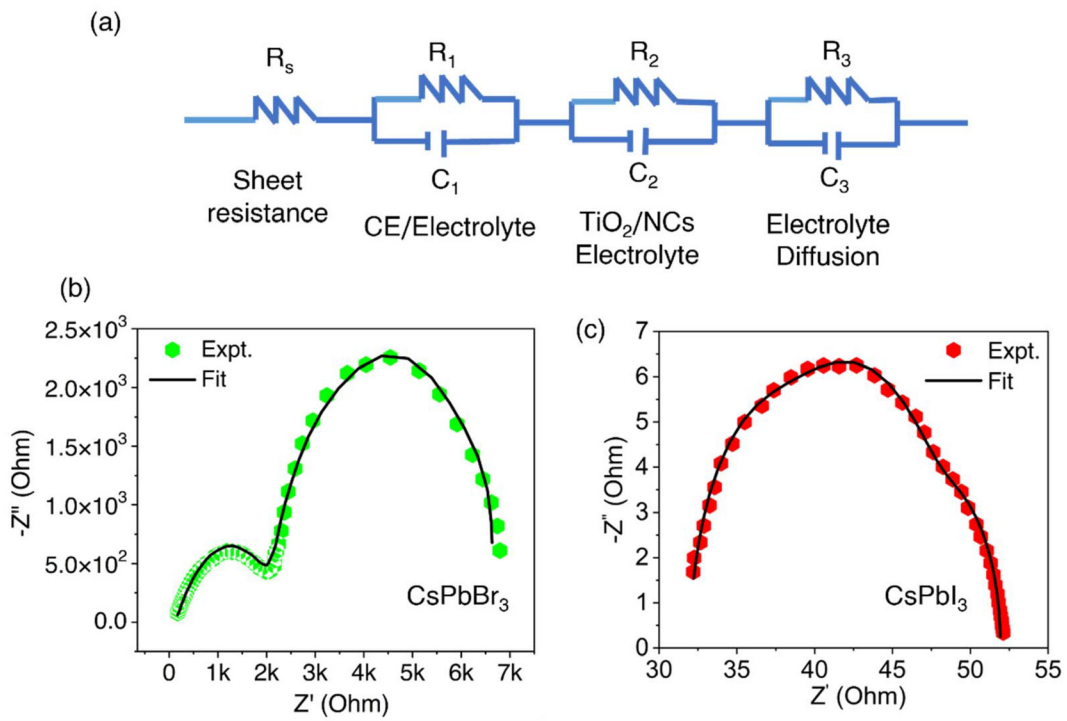

Fig. 5 Impedance spectroscopy (Nyquist plots) of the fabricated $CsPbI_3$ and $CsPbBr_3$-sensitized solar cells. (a) Equivalent circuit to fit the experimental data. Nyquist plots under illuminated conditions for (b) $CsPbBr_3$ and (c) $CsPbI_3$ solar cells.

Table 2 EIS fitting parameters of Nyquist plots in perovskite nanocrystal-sensitized solar cells

Sample	R_s (Ω)	R_1 (Ω)	R_2 (Ω)	R_3 (Ω)	C_1 (μF)	C_2 (μF)	C_3 (μF)
$CsPbI_3$	32.02	6.817	9.024	4.039	1.438	6.218	177.0
$CsPbBr_3$	75.00	80.00	2000	4800	0.0015	0.05	5.00

Table 3 Comparison of obtained PCE in $CsPbI_3$ nanocrystals-sensitized device with other reported DSSCs

Device structure	PCE	Ref.
TiO_2/N719 dye/$NiCo_2S_4$@rGO	8.5%	38
TiO_2/N-GQD/Pt	5.3%	39
TiO_2/DZ102:TZ101:JM102/$Co(Bpy)_3$	10.9%	40
Fe/S-TiO_2/N719/Au	6.46%	41
Cu_3VSe_4/m-TiO_2/N719/Pt	7.38%	42
TiO_2/$CsPbI_3$/Pt	12.5%	This work

explain the Nyquist plots, with three RC circuits in series corresponding to three interfaces, *i.e.*, electrolyte-counter electrode, TiO_2/QD, and diffusion of electrolytes across the mesoporous TiO_2.[37] The Nyquist plots of $CsPbBr_3$ and $CsPbI_3$ sensitized solar cells and the fitting of the data using the abovementioned model are shown in Fig. 5(b) and (c). The resulting fitting parameters are presented in Table 2.

From Table 2, we observe that all the values of resistance in $CsPbI_3$-sensitized solar cells are significantly lower than those in the $CsPbBr_3$-based device. As discussed earlier, a lower resistance implies more efficient charge injection from the sensitizer to the semiconductor and then from the semiconductor to the electrodes, thereby minimizing energy losses. From Table 2, it is also apparent that the capacitance values of different junctions in $CsPbI_3$-sensitized solar cells are also several orders higher in magnitude than their $CsPbBr_3$ counterparts. In PNCSSCs, a higher capacitance at the interfaces suggests more efficient charge storage and separation, reduced recombination rates, and improved carrier lifetimes. When carriers have a longer lifetime, they are more likely to reach the electrodes before recombining, which contributes to a higher FF by maintaining a robust current even at high voltage ranges. This prolonged carrier lifetime discerned through the low-frequency impedance spectrum in EIS, is essential for sustaining a high FF in devices with significant light absorption and carrier mobility. Lower R and higher C values in $CsPbI_3$ PNCSSCs result in a significantly higher fill factor (64%) than in $CsPbBr_3$-based (42%) PNCSSCs. A comparison of the efficiency of our fabricated devices with those reported in the literature is given in Table 3, showing the superior performance of $CsPbI_3$ nanocrystal-sensitized perovskite solar cells.

Conclusion

We have investigated cubic $CsPbBr_3$ and $CsPbI_3$ perovskite nanocrystals for their use as sensitizers for a superior alternative to degradable organic dyes in dye-sensitized solar cells. $CsPbI_3$ nanocrystals exhibit an absorption edge closer to the peak of the solar spectrum with a band gap of 1.8 eV in comparison to 2.4 eV for $CsPbI_3$ nanocrystals. In addition, a longer carrier lifetime of photogenerated charge carriers in $CsPbI_3$ (~130 ns) in contrast to $CsPbBr_3$ (~18 ns) and a favorable energy band alignment for charge transfer on mesoporous TiO_2 facilitates improved separation and collection of photogenerated carriers in the former. $CsPbI_3$-sensitized solar cells exhibit lower series shunt and charge transfer resistances but reveal much higher interface capacitance, leading to increased open-circuit voltage, short-circuit current density, and fill factor of the fabricated devices. Consequently, $CsPbI_3$-sensitized solar cells display a photoconversion efficiency of ~12.5%, significantly higher than the $CsPbBr_3$-sensitized (~3.9%) solar cells. Our results demonstrate the potential of solution-processed and highly luminous cubic phase $CsPbI_3$ NCs as efficient sensitizers and a compelling alternative to toxic and easily degradable dye-sensitized solar cells for low-cost solar energy harvesting applications.

Data availability

Data supporting this article have been included as part of the ESI.†

Conflicts of interest

The authors declare that they have no known competing financial interests or personal relationships that could have appeared to influence the work reported in this paper.

Acknowledgements

S. B. acknowledges the financial support from the Prime Minister's Research Fellow (PMRF) grant, Govt. of India. S. K. R. acknowledges the support of the DST-SERB project (CRG/2022/002316) grant and INAE Chair Professor fellowship. Dr Arup Ghorai, North Carolina University, is acknowledged for fruitful discussions.

References

1 H. A. Maddah, *Mater. Sci. Eng., B*, 2024, **302**, 117197.
2 C. S. Gaytán-Rivera, C. M. Díaz-Acosta, S. Estrada-Flores and A. Martínez-Luévanos, *Handbook of Emerging Materials for Sustainable Energy*, 2024, pp. 175–195.
3 M. Ayalasomayajula, M. Ravi Khurana, V. Balakrishnan, P. Shiva Chaudhary, S. Basu Bal and R. Kumar Baranwal, *IEEE J. Flexible Electron.*, 2024, **3**, 205–213.
4 S. M. Bonyad-Shekalgourabi and Z. Shariatinia, *Int. J. Hydrogen Energy*, 2024, **51**, 1397–1412.
5 H. H. Zeng, A. S. Rasal, M. Alemayehu Abate, A. Vithal Ghule and J. Y. Chang, *Chem. Eng. J.*, 2024, **495**, 153702.

6 S. Barzegari, A. R. Amani-Ghadim and F. Bayat, *Sol. Energy*, 2024, **277**, 112656.
7 S. U. Rahayu, Y. R. Wang, J. Bin Shi and M. W. Lee, *Sustainable Energy Fuels*, 2023, **8**, 113–124.
8 J. A. Carvalho Junior, C. L. Nunes, W. S. Machado and M. A. Schiavon, *Energy Technol.*, 2024, **12**, 2400254.
9 H. Emmanuel Sánchez-Godoy, T. López-Luke, I. Zarazúa, A. Herrera-Rodríguez, J. Castañeda-Contreras and R. Arturo Rodríguez-Rojas, *Sol. Energy*, 2024, **281**, 112818.
10 K. S. Velu, M. Sonaimuthu, M. Senthilkumar, N. Ahmad, S. Y. Alomar, J. Murugasamy, P. Ravisankar and Y. R. Lee, *Opt. Mater.*, 2023, **140**, 113895.
11 R. Johari, R. K. Sonker, O. Victor, Z. H. Khan, D. Aggarwal, S. Gupta and S. Kumar, *Macromol. Symp.*, 2023, **407**, 2200126.
12 S. V. Kuppu, M. Sonaimuthu, S. Marimuthu, S. Venkatesan, B. Murugesan, N. Ahmed, A. Karuppanan, P. Sengodu, A. R. Jeyaraman, S. Thambusamy and Y. R. Lee, *J. Mol. Struct.*, 2023, **1276**, 134763.
13 A. Ghorai, S. Mahato, S. K. Srivastava, S. K. Ray, A. Ghorai, S. Mahato, S. K. Srivastava and S. K. Ray, *Adv. Funct. Mater.*, 2022, **32**, 2202087.
14 B. Roy, S. Mahato, S. Bose, A. Ghorai, S. K. Srivastava, N. C. Das and S. K. Ray, *Chem. Mater.*, 2023, **35**, 1601–1609.
15 S. Mahato, A. Ghorai, S. K. Srivastava, M. Modak, S. Singh and S. K. Ray, *Adv. Energy Mater.*, 2020, **10**, 1–9.
16 S. Pal, A. Ghorai, S. Mahato and S. K. Ray, *Adv. Opt. Mater.*, 2023, **11**, 2300233.
17 S. Mahato, A. Ghorai, A. Mondal, S. K. Srivastava, M. Modak, S. Das and S. K. Ray, *ACS Appl. Mater. Interfaces*, 2022, **14**, 9711–9723.
18 S. Mahato, M. Tamulewicz-Szwajkowska, S. Singh, D. Kowal, S. Bose, J. Serafińczuk, K. Czyż, R. Jędrzejewski, M. D. Birowosuto, S. K. Ray and A. L. Abdelhady, *Adv. Opt. Mater.*, 2024, **12**, 2302257.
19 S. Krishnamurthy, P. Pandey, J. Kaur, S. Chakraborty, P. K. Nayak, A. Sadhanala and S. Ogale, *J. Phys. D: Appl. Phys.*, 2021, **54**, 133002.
20 S. Bose, S. Mahato, B. Roy, T. Singha, S. K. Srivastava and S. K. Ray, *ACS Appl. Nano Mater.*, 2024, **7**, 6020–6028.
21 L. Protesescu, S. Yakunin, M. I. Bodnarchuk, F. Krieg, R. Caputo, C. H. Hendon, R. X. Yang, A. Walsh and M. V. Kovalenko, *Nano Lett.*, 2015, **15**, 3692–3696.
22 L. Dai, Z. Deng, F. Auras, H. Goodwin, Z. Zhang, J. C. Walmsley, P. D. Bristowe, F. Deschler and N. C. Greenham, *Nat. Photonics*, 2021, **15**, 696–702.
23 D. Zhang, Y. Yu, Y. Bekenstein, A. B. Wong, A. P. Alivisatos and P. Yang, *J. Am. Chem. Soc.*, 2016, **138**, 13155–13158.
24 J. H. Noh, S. H. Im, J. H. Heo, T. N. Mandal and S. Il Seok, *Nano Lett.*, 2013, **13**, 1764–1769.
25 Q. Zhao, A. Hazarika, L. T. Schelhas, J. Liu, E. A. Gaulding, G. Li, M. Zhang, M. F. Toney, P. C. Sercel and J. M. Luther, *ACS Energy Lett.*, 2020, **5**, 238–247.
26 M. C. Brennan, S. Toso, I. M. Pavlovetc, M. Zhukovskyi, S. Marras, M. Kuno, L. Manna and D. Baranov, *ACS Energy Lett.*, 2020, **5**, 1465–1473.
27 S. Mandal, S. Mukherjee, C. K. De, D. Roy, S. Ghosh and P. K. Mandal, *J. Phys. Chem. Lett.*, 2020, **11**, 1702–1707.
28 E. Socie, B. R. C. Vale, A. Burgos-Caminal and J. E. Moser, *Adv. Opt. Mater.*, 2021, **9**, 2001308.
29 S. Pal, A. Ghorai, D. K. Goswami and S. K. Ray, *Nano Energy*, 2021, **87**, 106200.
30 S. Kajal, G. H. Kim, C. W. Myung, Y. S. Shin, J. Kim, J. Jeong, A. Jana, J. Y. Kim and K. S. Kim, *J. Mater. Chem. A*, 2019, **7**, 21740–21746.
31 Q. Qiao, J. Beck, R. Lumpkin, J. Pretko and J. T. Mcleskey, *Sol. Energy Mater. Sol. Cells*, 2006, **90**, 1034–1040.
32 C. Sima, C. Grigoriu and S. Antohe, *Thin Solid Films*, 2010, **519**, 595–597.
33 A. Hauch and A. Georg, *Electrochim. Acta*, 2001, **46**, 3457–3466.
34 Q. Wang, J. E. Moser and M. Grätzel, *J. Phys. Chem. B*, 2005, **109**, 14945–14953.
35 O. Amiri and M. Salavati-Niasari, *Mater. Lett.*, 2015, **160**, 24–27.
36 L. Han, N. Koide, Y. Chiba, A. Islam, R. Komiya, N. Fuke, A. Fukui and R. Yamanaka, *Appl. Phys. Lett.*, 2005, **86**, 1–3.
37 L. Han, N. Koide, Y. Chiba and T. Mitate, *Appl. Phys. Lett.*, 2004, **84**, 2433–2435.
38 K. Vanasundari, G. Mahalakshmi and K. Ravichandran, *J. Mater. Sci.: Mater. Electron.*, 2024, **35**, 1–12.
39 T. Dey, A. Ghorai, S. Das and S. K. Ray, *Sol. Energy*, 2022, **236**, 17–25.
40 M. Jiang, R. Wang, Z. Deng, G. Xu, Q. Shangguan, L. Sun, L. Zhang and X. Yang, *ACS Appl. Mater. Interfaces*, 2024, **16**, 51265–51273.
41 C. Y. Hsu, H. N. K. Al-Salman, Z. H. Mahmoud, R. M. Ahmed and A. F. Dawood, *Sci. Rep.*, 2024, **14**, 1–14.
42 N. Kaur, L. Biswal, A. Prieto, C. Y. Lai and D. R. Radu, *ACS Appl. Energy Mater.*, 2024, **7**, 5038–5049.